

THE ROLE OF DIFFUSIVE SHOCK ACCELERATION ON NONEQUILIBRIUM IONIZATION IN SUPERNOVA REMNANT SHOCKS II: EMITTED SPECTRA

DANIEL J. PATNAUDE¹, PATRICK SLANE¹, & JOHN C. RAYMOND¹, DONALD C. ELLISON²

Draft version June 5, 2018

ABSTRACT

We present a grid of nonequilibrium ionization models for the X-ray spectra from supernova remnants undergoing efficient diffusive shock acceleration. The calculation follows the hydrodynamics of the blast wave as well as the time-dependent ionization of the plasma behind the shock. The ionization state is passed to a plasma emissivity code to compute the thermal X-ray emission, which is combined with the emission from nonthermal synchrotron emission to produce a self-consistent model for the thermal and nonthermal emission from cosmic-ray dominated shocks. We show how plasma diagnostics such as the G' -ratio of He-like ions, defined as the ratio of the sum of the intercombination, forbidden, and satellite lines to the resonance line, can vary with acceleration efficiency, and discuss how the thermal X-ray emission, when the time-dependent ionization is not calculated self-consistently with the hydrodynamics, can differ from the thermal X-ray emission from models which do account for the hydrodynamics. Finally we compare the thermal X-ray emission from models which show moderate acceleration ($\sim 35\%$) to the thermal X-ray emission from test-particle models.

Subject headings: cosmic rays – thermal emission: ISM – shock waves – supernova remnant – X-rays: ISM

1. INTRODUCTION

In young supernova remnant (SNR) shocks, the acceleration of cosmic rays (CRs) leads to a softening of the equation of state in the shocked plasma. This comes about because the diffusive shock acceleration (DSA) process turns some non-relativistic particles into relativistic ones and because the highest energy relativistic particles escape from the shock. Both of these effects lead to lower post-shock plasma temperatures as well as higher post-shock densities (e.g., Jones & Ellison 1991; Berezhko & Ellison 1999). The ionization of shocked gas at a particular time depends upon both the gas density and the electron temperature, and it has been recently shown by Patnaude et al. (2009) that the time-dependent nonequilibrium ionization (NEI) and electron temperature, T_e , are influenced by the DSA efficiency, ϵ_{DSA} .

A number of young SNRs show some evidence for both nonthermal and thermal emission behind the forward shock, including SN 1006 (Vink et al. 2003; Bamba et al. 2008), Tycho (Hwang et al. 2002), Kepler (Reynolds et al. 2007), and recently Cas A (Araya et al. 2010). The thermal emission arises when the forward shock sweeps through the circumstellar medium (CSM) and heats it to X-ray emitting temperatures. As pointed out in Ellison et al. (2007), the thermal X-ray emission is often considerably fainter than the nonthermal emission, but there exist examples where the thermal emission is as bright or brighter than any nonthermal emission, such as in parts of RCW 86 (Vink et al. 2006) and N132D (Xiao & Chen 2008). In contrast, in SNR RX J1713.7-3946, the lack of thermal X-ray emission is an important constraint on the ambient medium density, and we have

recently shown that if the TeV γ -ray emission is hadronic in origin, then copious thermal X-ray emission would be observed with current X-ray observatories (Ellison et al. 2010).

Here we extend our previous work (Patnaude et al. 2009; Ellison et al. 2010) by coupling our models to a plasma emissivity code, producing thermal X-ray spectra and ionization timescale parameters (*i.e.* $n_e t$) as a function of position and time in the SNR shock. Again, as in Patnaude et al. (2009), we limit our analysis to the region between the forward shock (FS) and contact discontinuity (CD). In § 2 we present our new model and outline how we have coupled our hydrodynamical model to a plasma emissivity code. The inclusion of the hydrodynamical evolution makes it difficult to compare the computed thermal emission to existing models, since the shocked, ionizing plasma is expanding adiabatically and the electron temperature is constantly evolving. To test the code, we present in § 2 a test where we follow the ionization in the case of a fixed density and temperature, which is equivalent to available NEI models in spectral fitting codes such as XSPEC.

The parameter space involved in producing the thermal and nonthermal emission as well as the hydrodynamical evolution is extensive and in § 3 we show a simplified set of models where we only vary a subset of parameters such as the shock acceleration efficiency. In this section, we show how the so called G -ratio, which is a measure of electron temperature, varies with acceleration efficiency. We find that since the increased acceleration efficiency generally leads to lower electron temperatures, increasing the acceleration efficiency results in higher G -ratios. In § 4, we compare our models to similar models where the X-ray emission is calculated not from the ionization state of each element, but from the ionization timescale which the shocked gas is expected to have at the end of the simulation. We find that the results differ, mainly at lower energies. Finally in § 4 we discuss the recent

¹ Smithsonian Astrophysical Observatory, Cambridge, MA 02138

² Physics Department, NC State University, Box 8202, Raleigh, NC 27695; don_ellison@ncsu.edu

result by Berezhko & Völk (2010) and show that the absence of thermal X-ray emission does not naturally lead to the interpretation that the TeV gamma-ray emission is hadronic in origin. We argue that if the blastwave has only recently hit the circumstellar shell, then the shocked gas, though at X-ray emitting temperatures, will be underionized. We show that our results and those of Ellison et al. (2010) are consistent with the material being at a lower density.

2. EMISSIVITY CODE

In previous papers (Ellison et al. 2007; Patnaude et al. 2009; Ellison et al. 2010), we outlined our model which coupled the NEI calculation to the cosmic ray acceleration and hydrodynamics code. For each simulation cell and timestep, we calculate an ionization state vector $f(X^i)$, an electron temperature T_e , and electron and ion densities, n_e and n_i . Combined with a chosen set of abundances (here we choose those of Anders & Grevesse (1989)), these quantities are all that is required as input to produce the thermal X-ray emission. As in Patnaude et al. (2009), the ionization processes included in our NEI calculation include direct collisional ionization and collisional excitation followed by autoionization. Additionally, the recombination rates include radiative recombination and dielectronic recombination. We neglect Auger ionization as well as photoionization. In the current version of our code, we do not include ionization from super-thermal particles; in an ionizing plasma, these effects are expected to be small (Porquet et al. 2001a).

We have chosen to couple our models to an updated version of the Raymond–Smith emissivity code (RS93; Raymond & Smith 1977; Brickhouse et al. 1995). RS93 differs from other available codes in terms of the number of included emission lines, a few line centroids, and individual line emissivities. These differences are sufficiently numerous to make it difficult to compare our calculated spectra to other available models such as APED, but the differences are well documented (c.f., Smith et al. 2001). Additionally, since our models not only follow the time dependent ionization, but also are dynamical in nature, it is not adequate to compare the calculated spectra to existing models such as `nei` and `pshock` in XSPEC.

To determine whether the modeled spectra are consistent with existing NEI calculations, as well as consistent with models in collisional ionization equilibrium, we performed the following test: we ran a simulation for a prescribed amount of time, and far upstream from the shock, we fix the electron temperature at a constant value of $T_e = 3 \times 10^6$ K and keep the density fixed at $n_{p,0} = 3.0 \text{ cm}^{-3}$. That is, while in general the hydrodynamics computes the electron temperature and densities self-consistently behind the shock, for the purposes of this test we keep the electron temperature at a high, constant value far enough upstream of the shock so that we can evolve the NEI. This is equivalent to the single temperature, single ionization age models found in XSPEC, such as `nei` and `vnei`. We compare our computed spectrum to both what is computed in the XSPEC model as well as a model for a plasma in collisional ionization equilibrium (e.g. `raysmith` or `mekal`). For simplicity, we limited our calculations to spectra that only include H, He, and Si. In Figure 1, we show the computed and reference spectra

for a shocked plasma that has been evolving for 500 yrs, as well as what the same spectrum looks like under conditions of collisional ionization equilibrium. In the top panel of Figure 1, we also plot the evolution of Li- and He-like ions of silicon.

At an age of 500 years, corresponding to an ionization age of $\sim 5 \times 10^{10} \text{ s cm}^{-3}$, at an assumed density of $n_{p,0} = 3.0 \text{ cm}^{-3}$, we observe emission lines from several atomic transitions. For instance, from the helium iso-sequence, we see line emission at 2.295 keV ($1s^2 - 1s4p$), 2.185 keV ($1s^2 - 1s3p$) 1.866 keV ($1s^2 - 1s2p$), and the multiplet transitions $1s^2 - 1s2p^3P^0$ at 1.85 keV and $1s^2 - 1s2s^3S$. Also, at lower energies we see numerous emission lines from the lithium to nitrogen iso-sequences, including multiplet transitions which lead to multiple spectral lines.

In Figure 2, we plot the same model ($T_e = 3 \times 10^6$ K and $n_{p,0} = 3.0 \text{ cm}^{-3}$) at an age of 2500 yrs. After 2500 years, the same helium-like lines are seen as in the $t_{\text{SNR}} = 500$ year model, but the intensities have increased relative to the lower ionization states. This is reflected in the top panel of Figure 2, where the lithium-like state of silicon is approaching the collisional ionization equilibrium value of ~ 0.1 (at $T_e 3 \times 10^6$ K.) Likewise, in collisional ionization equilibrium at 3×10^6 K, the He-like state is populated at ~ 0.87 (in fact, in collisional ionization equilibrium, Li- and He-like states are the dominant species at this temperature for silicon, with additional contributions from the Be-like state; a negligible fraction of ions are in the H-like state), and the NEI conditions shown here are seen to be approaching it after 2500 years.

In both test cases, the computed and reference NEI spectra are in good agreement, showing the same underlying continuum and similar line emission, with differences most noticeable in the emission lines between 200 and 500 eV. We attribute these differences to small differences between the underlying atomic data used in the codes. The most obvious difference between the two is seen as the obvious lack of an emission line in the XSPEC `nei` model at ~ 350 eV (Si XII n=2 to n=4 multiplet). In the $t_{\text{SNR}} = 500$ year model, this line is quite bright, while in the higher aged model it appears to be weakening, relative to the surrounding lines (which are also weaker, relative to the continuum).

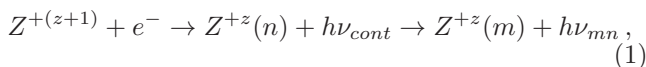
The goal of this testing was to ensure that the NEI calculation in our model, in the limit of a single ionization age, single temperature `nei` model, is consistent with existing models. Realizing that there are differences in the underlying atomic data that will be manifest in the existence and intensity of individual emission lines (in particular, the `nei` model includes many more emission lines from He-like states, as seen in Figures 1 and 2), our aim was to track the trending in the two NEI models to ensure that they behave consistently against one another. As an additional test, we chose to compare our spectrum to that from a plasma in collisional ionization equilibrium. We find that, as expected, the computed NEI is in fact approaching the CIE spectrum expected for the temperature and density we are using for the test (Smith & Hughes. 2010).

3. RESULTS

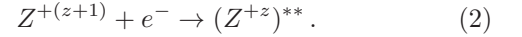
The cosmic ray hydrodynamics code contains an extensive set of parameters which affect the SNR dynamics, emitted thermal and nonthermal broadband spectrum, and relativistic particle populations. An exhaustive study of the effects that all these parameters have on the emitted spectrum is beyond the scope of this paper, but we note that combinations of parameters have been successfully used to produce emitted spectra from SNR RX J1713.7-3946, ruling out certain models for that SNR (Ellison et al. 2010). To simplify the process, we choose a set of models where we only vary the acceleration efficiency ϵ_{DSA} and ambient medium density, and leave everything else fixed. We note that the application of these models to a specific SNR would require a very specific set of parameters, so we restrict ourselves to phenomenological studies for now.

Our model assumes the following set of parameters: $t_{\text{SNR}} = 1000$ yr, $E_{\text{SN}} = 10^{51}$ erg, and $M_{ej} = 1.4M_{\odot}$. Additionally, we assume an exponential ejecta profile and an ambient magnetic field of $15\mu\text{G}$. Parameters which affect the ionization calculations and resultant thermal emission include the assumed abundances and the electron heating. We assume cosmic abundances (Anders & Grevesse 1989) and heating via Coulomb collisions. The ambient medium has a temperature of 10^4 K and is preionized at 10%. We vary the acceleration efficiency, ϵ_{DSA} between 1% (test particle) and 75%, and except where indicated otherwise, we chose ambient medium densities, $n_{p,0} = 0.1, 0.3, 1.0, \text{ and } 3.0 \text{ cm}^{-3}$. Our model also includes the ability to apply interstellar absorption as well as combine the thermal and nonthermal emission. For clarity, we do not include any absorbing column, and except where noted, we neglect the contribution to the spectrum by the nonthermal continuum. We note, as in SNR RX J1713.7-3946, that the underlying nonthermal continuum can be the dominant source of X-ray photons, so the models like those presented here are most appropriate for comparison with emission line fluxes for shocks that show a combination of thermal and nonthermal emission.

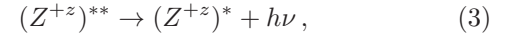
The emitted thermal spectrum is a combination of bremsstrahlung and two photon continua and line radiation. The formation of lines mainly occurs by electron impact of atoms or ions. The excitation can generally be broken down into excitation of outer-shell electrons, excitation of inner-shell electrons, and resonant excitation (Raymond & Brickhouse 1996). Additional contributions from radiative recombination to excited states, dielectronic recombination satellite lines and inner shell ionization are sometimes significant, especially in plasmas out of ionization equilibrium. In the process of radiative recombination, the following occurs with



where the ion $Z^{+(z+1)}$ captures an electron and is de-excited to the m -th excited state via emission of a photon. In the process of dielectronic recombination, a free electron gains kinetic energy as it approaches an ion, then excites a bound electron to an energy level higher than the energy it had at infinity, so the free electron is captured to form a doubly excited state of ion Z^{+z} ,



If auto-ionization occurs (the reverse of the capture process) the system returns to its original state and no recombination takes place. Alternatively a fraction of the ions in the autoionizing state decays by spontaneous radiative transition of the inner excited electron to a state below the first ionization limit:



where the stabilizing transition in the recombined ion Z^{+z} results in the emission of a dielectronic satellite line of the parent transition in the recombining ion $Z^{+(z+1)}$. Eventually, the singly excited state cascades down to the ground state with subsequent emission of photons.

3.1. Emission Line Diagnostics

To demonstrate a potentially useful diagnostic predicted by the models that should be observable by *Astro-H*, we consider the $n=2 \rightarrow n=1$ emission of He-like ions. This consists of a resonance (r) $2^1P \rightarrow 1^1S$ line, a forbidden (f) $2^3S \rightarrow 1^1S$ line, and an intercombination (i) $2^3P \rightarrow 1^1S$ line. The intensity ratio $(f+i)/r$, called the G -ratio, varies with density, ultraviolet radiation intensity, temperature and ionization state. The shocked, swept-up material behind SNR shocks is considered to be at a low enough density ($n_e \ll 10^{10} \text{ cm}^{-3}$), and the UV radiation field is sufficiently negligible, that density dependent variations in the spectra are not observable. Therefore we will consider only the variation with temperature and ionization state. As a point of reference, the G -ratio decreases with increasing electron temperature (Gabriel & Jordan 1969). Finally, we note that there are a number of satellite lines (s) formed by transitions of the form $1s2s^2 \rightarrow 1s^22s$, $1s2s2p \rightarrow 1s^22p$ and $1s2p^2 \rightarrow 1s^22p$ which lie at wavelengths near the i and f transitions. Since current and near term observations are unable to resolve their contributions to the spectrum, we define an observable ratio $G' = (f+i+s)/r$.

The lines in the G' -ratio contain contributions from direct collisional excitation by electrons (f, i and r), radiative and dielectronic recombination of the H-like ion into the excited levels (f, i and r), dielectronic recombination of the He-like ion (s), innershell excitation of Li-like and lower ions (s) and innershell ionization of Be-like and lower ions (s).

Since the resultant emitted thermal X-ray spectrum can be quite complicated, containing emission lines from H- and He-like states as well as a forest of emission lines from intermediate charge states (e.g. as was demonstrated in Figures 1 and 2), we focus on the bulk characteristics of the emitted spectrum. To do this, we sum the emitted spectrum from the contact discontinuity to forward shock and investigate the global characteristics of the thermal emission as a function of both acceleration efficiency, and to a lesser extent the ambient medium density.

In Figures 3 – 6 we plot the G' -ratio for the He-like states of oxygen, neon, magnesium, and silicon. Because excitation cross sections for the forbidden and intercombination lines decrease with energy, relative to that of the resonance line, and because the cross sections for the

forbidden and intercombination lines have strong resonance contributions near the excitation threshold, G' can be thought of as a diagnostic of the electron temperature. In addition, the dielectronic recombination satellites are excited by electrons well below the threshold for exciting the r line, but since they are observed near the triplet state (where they remain unresolved with current instrumentations), their contribution to the flux should be included, thus weakening the overall dependence upon temperature. The G' -ratio also depends upon the ionization state of the gas, since the triplets are populated by recombination from the H-like states, and innershell excitation and ionization of lower charge states also contribute. The interplay of temperature and ionization state requires a fully time-dependent ionization model such as we present here, and this ratio will be an important diagnostic tool for upcoming missions such as *Astro-H*. We note that we have so far neglected excitation and ionization by the nonthermal electrons (e.g. Porquet et al. (2001a)), and that some improvements to the atomic rates in our code remain to be implemented (e.g., Porquet et al. (2001b)), but that we expect the trends of the predictions to be reliable.

In Patnaude et al. (2009) we showed that the electron temperature varied roughly inversely with the acceleration efficiency, that is, as acceleration efficiency increases, the electron temperature decreases. Therefore, in order to understand how the G' -ratio changes, we plot it versus the acceleration efficiency, rather than electron temperature. In Figure 3, we show the variations in G' of oxygen with acceleration efficiency, at constant density. At high ambient densities G' behaves as expected. That is, G' increases with increasing efficiency (or, equivalently, increases with decreasing temperature). However, the lowest density ambient medium model shows the opposite trend, except at the highest acceleration efficiencies, where G' is seen to rise rapidly. Similarly, in neon, as seen in Figure 4, the G' -ratio decreases with increasing efficiency for $n_{amb} = 0.1 \text{ cm}^{-3}$. However, at a density of 0.3 cm^{-3} , the trend with acceleration efficiency is consistent with the high density results for oxygen. A similar result is seen for magnesium, while in silicon, the variation in G' at $n_{amb} = 0.1$ and 0.3 cm^{-3} is opposite to that seen in the higher density models (compare the upper two panels of Figure 6 to the bottom two). The decline in G' with acceleration efficiency in the lower density models can be understood as an effect of the underionization of the plasma. An increase in acceleration efficiency leads to a higher compression ratio, and since the ionization rates of ions below He-like are not very sensitive to temperature for these ions at the temperatures of these models, the higher acceleration efficiency models reach higher He-like ionization fractions. This increases the strength of the resonance line relative to the inner shell excitation lines.

3.2. Global Properties

To better understand the variations seen in G' with ϵ_{DSA} , we plot in Figures 7–8 the variation in G' as a function of weighted electron temperature, at constant ambient medium density. The weighted electron temperature is over the entire region between the forward shock and contact discontinuity, and we weight the electron temperature in each hydrodynamical cell by the emission

measure of the cell (i.e. $\langle T_e \rangle = \text{EM}^{-1} \sum_i (T_e^i \times \text{EM}^i)$). The emission measure may not be the best quantity to weight the temperature by, and it may be more meaningful to weight the temperature by the power in the He-like triplet, but that will result in a weighted temperature which varies with element, such that the average temperature as derived from the He-like oxygen will be different from the average temperature as derived by silicon. Using the emission measure to weight the temperature allows us to compare how G' varies with T_e for each element, and also compare how it varies between elements. We note that the emission measure in each cell is the only quantity related to the emitted spectrum which will not vary with element.

In Figure 7 we plot G' versus T_e for O, Ne, Mg, and Si, at constant ambient medium density. The emission measure weighted average electron temperature for the shocked CSM varies from $\sim 7 \times 10^6 \text{ K}$ ($\sim 600 \text{ eV}$) in the highly efficient models to $> 10^7 \text{ K}$ ($\sim 850 \text{ eV}$) in the test particle models. The curves are complicated; in the top panel, O is seen to decrease initially with increasing $\langle T_e \rangle$ before increasing above $9 \times 10^6 \text{ K}$. However, everywhere the resonance line intensity is well above the sum of the forbidden, intercombination, and satellite lines ($G' < 1$). In neon, again the resonance line is brighter than the other contributions, while in magnesium and silicon, the flux from the forbidden, intercombination, and satellite lines is greater than for the resonance line, and increases with increasing temperature (i.e. decreasing acceleration efficiency).

Generally, the G' -ratio is sensitive to temperature; at high temperatures, all states are collisionally excited, but at lower temperatures, dielectronic recombination becomes important. The triplet states will be preferentially populated through recombinations simply because of their greater statistical weight, thus increasing the intercombination and forbidden line strengths relative to the resonance line. This is seen in the low temperature (high acceleration efficiency) end of Figure 8, where the G' -ratio is highest. This is not, however, the case for the lower density model. Here, the G' -ratio is generally seen to be highest in the test particle model.

To understand the differences between Figure 7 and 8, we plot in Figure 9 the average charge state for silicon and oxygen. Two trends are immediately clear from this plot. First, in the low density case, the average charge state for silicon is well below the He-like state, but the average charge state increases with acceleration efficiency. Additionally, a higher ambient medium density results in a higher average charge. This is because the higher density behind the shock increases the collisional ionization rate, and this dominates over the temperature dependence of the ionization rates of Si XII and lower ions. At the highest densities, the average charge is much higher, and it *decreases* with increasing efficiency. In this case, the decline in temperature with acceleration efficiency decreases the ionization rate of Si XIII, and this dominates over the increase in density because of the high ionization potential of He-like Si XIII. As seen in Figure 9 similar trends are seen in oxygen. Here, however, even at the highest efficiencies in the high density cases, oxygen is almost fully ionized.

Equating these results to Figures 7 and 8 means that

in the low density case (Fig. 7), the lower density implies less collisional ionization and less efficient Coulomb heating, so that the plasma stays less ionized. More precisely, in the low density models, the He-like states are not reached, and forbidden line emission is dominated by inner shell excitation of lower ions. In higher density models, the He-like states are reached, and the expected dependence with temperature is seen (c.f. Fig. 8). We stress that in the low density models, some elements, such as silicon, will be highly underionized and the He-like triplets will be quite faint. These lines will be hard to detect, and when combined with any nonthermal continuum emission, they might be undetectable with current instrumentation.

We end this section with Figure 10, a plot of the variation in G' , average charge state, and electron temperature as a function of ambient medium density, at constant acceleration efficiencies. This plot shows how these values vary between the test particle case and a 50% efficient shock. As expected, the average electron temperature in the test particle case is higher than in the efficient case, but the average charge states are very similar. The biggest differences come from the ratio of G' , where in the low density models, the G' -ratio is higher in the test particle case than in the efficient case, while above a density of $\lesssim 1.0 \text{ cm}^{-3}$, the relation is reversed, with the G' -ratio in the efficient case is higher. From this plot, it is clear that at identical ambient medium densities, similar charge states can result between the efficient and inefficient models, while the temperatures can differ by $\sim 30\%$ and the line ratios can differ by $\sim 10\%$. For instance, for an ambient medium density of 1.0 cm^{-3} , the weighted temperature in the 50% efficient model is 30% lower than in the test particle case. However, the ionization state for silicon here is virtually identical, but the G' -ratio in the efficient model is 10% higher than in the inefficient model. At temperatures which can differ by as much as they do in Figure 10, what we see here is that at constant ambient medium density but differing efficiencies, different lines are seen at different intensities. Since the line ratios and underlying electron temperatures are different between the efficient and inefficient models, the shape of the resultant spectra will differ.

4. DISCUSSION

The models presented here differ from existing available models that compute the X-ray emission from shocks in several ways, but the relevant difference here is that the nonequilibrium ionization is followed simultaneously with the shock dynamics and particle acceleration. The ionization vector is then passed directly to an emissivity code to compute the thermal X-ray emission. Since the NEI is evolved simultaneously with the hydrodynamic evolution, our calculation includes changes to the NEI as a result of adiabatic losses, or as is the case in an efficient model, increased compression behind the shock resulting from efficient shock acceleration.

To illustrate this effect, in Figure 11, we compare the thermal X-ray emission from models where we follow the time-dependent ionization with the hydrodynamics (black curves) to the thermal X-ray emission from models where we calculate the ionization structure from the final ionization age (τ) and electron temperature (red curves). Here, the final ionization for each cell age is de-

finied as the τ at the end of the simulation. Then, for comparison, we re-run the NEI calculation for the final electron temperature and the time equivalent to the age of the SNR at the end of the hydrodynamical simulation. For these models, we do not include any efficient particle acceleration, as that will only complicate the interpretation of these results. Computing the ionization structure in each grid cell from the final τ is similar to assuming a single τ , single T_e model for each cell in XSPEC (e.g. the `nei` model), except that in our computation of τ and T_e in the hydrodynamics, we still account for adiabatic cooling in the shocked gas, since these values were computed initially from the hydrodynamics. This approach is similar to Ellison et al. (2007). As seen in Figure 11, there are differences between the two resultant spectra. In the low density ($n_{p,0} = 0.1 \text{ cm}^{-3}$) model, the calculation of the emitted spectrum from the final ionization age slightly overpredicts the final thermal X-ray emission, most evidently seen around the He-like lines of magnesium and silicon, as well as from the emission of L-shell iron. Not surprisingly, the shape of the underlying continua are consistent. This is expected because the shape of the continuum is determined by the electron temperature, which are identical between the two models.

In the higher density ($n_{p,0} = 1.0 \text{ cm}^{-3}$) model, the differences are much larger, particularly at low energy. In particular, the ionization state and thermal X-ray emission computed from the final ionization age and temperature underpredict the Fe-L emission. We interpret this difference as being a direct result of not following the ionization explicitly; that is, when computing the ionization state from a single density and Δt , intermediary ionization states are not correctly populated, since the calculation assumes that the shocked gas has gone from a cold (10^4 K) gas to hot (several 10^{6-7} K) in a single timestep. We note that were a spectrum like this fit with existing models, it would appear that the shocked plasma is overabundant in metals such as argon and calcium. Figure 11 clearly demonstrates the need to compute the ionization self-consistently with the shock hydrodynamics (regardless of whether one considers the effects of efficient diffusive shock acceleration).

4.1. Efficient vs. Inefficient Models

In Figure 12, we plot the observed differences between the thermal emission from a test-particle model and the combined thermal and nonthermal emission from an efficient model. The black crosses in Figure 12 are simulated data for a 50 ksec Chandra ACIS-S observation of an SNR with $\epsilon_{\text{DSA}} = 0$ and $n_{p,0} = 0.3 \text{ cm}^{-3}$. The blue curve is the nonthermal emission, the red curve is the thermal emission and the black curve is their sum. In the efficient model, we assume $\epsilon_{\text{DSA}} = 35\%$ and $n_{p,0} = 0.3 \text{ cm}^{-3}$. As expected, at the high energy end, the nonthermal emission dominates the shape of the spectrum. However, below about 2 keV, where the thermal emission is comparable to the nonthermal emission, differences are still seen.

Below 1 keV, the thermal emission is \sim an order of magnitude above the nonthermal emission. It is in this regime where the differences between the thermal emission from an efficient model and a test particle model are most apparent. In particular, the emission from oxygen

is seen to differ between these two models, and is reflected in the fit residual, shown in the lower panel, which shows that the modeled thermal emission from the efficient case does not accurately describe the thermal emission in the test particle case. This suggests that the emission lines contribute at differing levels between the efficient and inefficient models.

4.2. Comparisons to Recent Calculations for Limits on the Thermal X-ray Emission in RX J1713.7-3946

Recently, Berezhko & Völk (2010) used models from Hamilton et al. (1983) to constrain the origin of the TeV γ -ray emission in RX J1713.7-3946. They argued that, based on fits to the broadband nonthermal continuum, the TeV γ -ray emission is hadronic in origin, with $\sim 35\%$ of the shock kinetic energy being deposited into nuclear cosmic rays. However, Ellison et al. (2010) argue that if the TeV γ -ray emission were hadronic in origin, thermal X-ray emission would be detected, though the model used there is for a constant ambient medium density of 0.2 cm^{-3} , for the hadronic scenario. In the model developed by Berezhko & Völk (2010), the SNR blastwave has been expanding through a low density ($n_H \approx 0.0008 \text{ cm}^{-3}$) bubble and has recently encountered the bubble wall, with $n_H = 0.25 \text{ cm}^{-3}$ at present. From their model, we estimate that the shock began encountering the bubble wall ~ 800 years ago, as determined by the curve for N_g in the top panel of their Figure 1 (Berezhko & Völk 2010). They assume that the thermal X-ray emission as determined for the Sedov solution by Hamilton et al. (1983) is reduced by an amount equivalent to the ratio of the bubble emission measure to the Sedov emission measure, here equal to 0.46 (Berezhko & Völk 2010). Additionally, they assume a value of $\eta = 8 \times 10^{49}$, where $\eta = n^2 E_{\text{SN}}$ (Hamilton et al. 1983). Their chosen value of η corresponds to an explosion energy of 1.3×10^{51} erg and an ambient medium density of 0.25 cm^{-3} . They use the value of η and an assumed electron temperature of 1 keV to estimate the thermal X-ray emission from the recently shocked bubble wall, and they find that at 1 keV, the thermal X-ray emission is approximately half the nonthermal flux (Berezhko & Völk 2010).

Since the blastwave hit the bubble wall ~ 800 years ago and the electron temperature is ~ 1 keV, the shocked plasma will be underionized. This is probably best illustrated in Figure 10, where for an ambient medium density of 0.25 cm^{-3} , the average charge state of silicon is quite low, and in fact since the model shown in Figure 10 is for a constant density model, it represents an upper limit on what the ionization state would be in Berezhko & Völk (2010). Thus, the shocked plasma from the bubble wall will likely be underionized.

Basically, Berezhko & Völk (2010) use a model for thermal X-ray emission from a Sedov-like SNR (of age 1600 yr and distance 1 kpc, but renormalized to match the emission measure of a shocked shell) to the emission from a recently shocked thin shell undergoing efficient particle acceleration. As we showed above, however, The emitted spectra in the two scenarios are expected to be markedly different. We stress that in order to constrain the origin of the TeV gamma-ray emission, whether it arises from either leptonic or hadronic sources, the time-dependent ionization and thermal X-ray emission must

be calculated in a self-consistent manner with the shock acceleration and hydrodynamics, as was done for a simple case in Ellison et al. (2010).

As was shown in previous sections, the increased compression from the shock acceleration increases the line intensities (from oxygen and neon, for instance), so Berezhko & Völk (2010) will underestimate the contributions of line emission to the total flux. This is consistent with Ellison et al. (2010) where both a low ambient medium density and a high electron-to-proton ratio at the maximum energies were required in order to hide any emission lines and still fit the shape of the GeV–TeV continuum.

Since the shock acceleration does have an effect on the ionization balance and thus the emitted thermal X-ray spectrum, using thermal X-ray emission models which do not account for increased ionization or compression when trying to understand the origin of GeV–TeV emission is not accurate. This will be of particular importance when the blastwave is moving through complex environments such as circumstellar shells, where the density can change by a few orders of magnitude over relatively small spatial scales. In SNR RX J1713.7-3946, the absence of thermal X-ray emission rules out a hadronic origin to the γ -ray emission in the case of expansion into a uniform circumstellar medium (Ellison et al. 2010). Additional modeling will be required to assess whether or not the hadronic origin to the TeV emission is a viable picture under other, more complex conditions.

5. CONCLUSIONS

We have presented an extensive grid of models where we study the effects on the emitted thermal X-ray spectrum behind SNR shocks. To accomplish this, we have coupled our CR-Hydro+NEI calculation to an updated version of the Raymond–Smith plasma emissivity code. In studying the global properties of the shocked plasma, we find that in the low density limit, the plasma temperature diagnostic, the G' -ratio, decreases with decreasing temperature (increasing acceleration efficiency) for higher Z elements such as magnesium and silicon. This is opposite to the behaviour at higher densities, where the G' -ratio increases with decreasing temperature, as expected. We find that the reason for this behavior is that in the lower density models, the electron temperatures are lower, but more importantly, the ions do not reach the higher ionization states. Additionally, we find that in low density models, the average charge states increase with increasing efficiency, while at higher densities, the charge state is seen to decrease. This is because in the low density model, the higher efficiency leads to higher post shock densities and therefore more collisional excitation, while in the high density models, the shocked plasma does not reach as high a temperature in the efficiently accelerating models, so the ions are less ionized, even though the post shock density is also high. The differences in average charge state between the low and high density models are thus viewed as a result of the temperatures in the low density model generally being higher than in the high density model.

Based on our results, we conclude that it is not sufficient to calculate the ionization state of the plasma as a “post-processing” step. While in lower density models the differences are small, at higher densities, the calcu-

lation will underpredict the emission from intermediate charge states, particularly emission from Fe-L. We speculate that these differences might be even larger in metal rich ejecta where the number of free electrons will be large. Finally, we note that the shape of the emitted spectrum in an efficient model, even when folded through a CCD-resolution response, is fundamentally different than the emitted spectrum from a test-particle model.

D. J. P. acknowledges support from *Chandra* Theory grant TM0-11006A, and P. O. S. and D. J. P. acknowledge support from NASA contract NAS8-03060. D.C.E. acknowledges support from NASA contracts ATP02-0042-0006, NNH04Zss001N-LTSA, and 06-ATP06-21. The authors are grateful to the KITP in Santa Barbara where part of this work was done when the authors were participating in a KITP program.

REFERENCES

- Aharonian, F. A. et al. 2007 (HESS collaboration), *A&A*, 464, 235
- Anders, E., & Grevesse, N. 1989, *Geochim. Cosmochim. Acta*, 53, 197
- Araya, M., Lomiashvili, D., Chang, C., Lyutikov, M., & Cui, W. 2010, *ApJ*, 714, 396
- Bamba, A., et al. 2008, *Advances in Space Research*, 41, 411
- Berezhko, E. G. & Ellison, D. C. *ApJ*, 526, 385
- Berezhko, E. G., & Völk, H. J. 2010, *A&A*, 511, A34
- Borkowski, K. J., Lyerly, W. J., & Reynolds, S. P. 2001, *ApJ*, 548, 820
- Brickhouse, N. S., Raymond, J. C., & Smith, B. W. 1995, *ApJS*, 97, 551
- Cassam-Chenaï, G., Hughes, J. P., Ballet, J., & Decourchelle, A. 2007, *ApJ*, 665, 315
- O’C. Drury, L., Aharonian, F. A., Malyshev, D., & Gabici, S. 2009, *A&A*, 496, 1
- Dwarkadas, V. V. 2000, *ApJ*, 541, 418
- Ellison, D. C., Patnaude, D. J., Slane, P., & Raymond, J. 2010, *ApJ*, 712, 287
- Ellison, D. C., & Cassam-Chenaï, G. 2005, *ApJ*, 632, 920
- Ellison, D. C., Patnaude, D. J., Slane, P., Blasi, P., & Gabici, S. 2007, *ApJ*, 661, 879
- Ellison, D. C., Slane, P. & Gaensler, B. M. 2001, *ApJ*, 563, 191
- Gabriel, A. H., & Jordan, C. 1969, *MNRAS*, 145, 241
- Gottlieb, E. V., Koralesky, B., Rudnick, L., Jones, T. W., Hwang, U., & Petre, R. 2001, *ApJ*, 552, L39
- Hamilton, A. J. S., Chevalier, R. A., & Sarazin, C. L. 1983, *ApJS*, 51, 115
- Helder, E. A., & Vink, J. 2008, *ApJ*, 686, 1094
- Hwang, U., Decourchelle, A., Holt, S. S., & Petre, R. 2002, *ApJ*, 581, 1101
- Jones, F. C. & Ellison, D. C. 1991, *Space Sci. Rev.*, 58, 259
- Katz, B. & Waxman, E. 2008, *JCAP*, 1, 18
- Mazzotta, P., Mazzitelli, G., Colafrancesco, S., & Vittorio, N. 1998, *A&AS*, 133, 403
- Morlino, G., Amato, E., & Blasi, P. 2009, *MNRAS*, 392, 240
- Patnaude, D. J., Ellison, D. C., & Slane, P. 2009, *ApJ*, 696, 1956
- Porquet, D., Arnaud, M. & Decourchelle, A. 2001, *A&A*, 373, 1110
- Porquet, D., Mewe, R., Dubau, J., Raasen, A.J.J. & Kaastra, J.S. 2001, *A&A*, 376, 1113
- Raymond, J. C., & Smith, B. W. 1977, *ApJS*, 35, 419
- Raymond, J. C., & Brickhouse, N. S. 1996, *Ap&SS*, 237, 321
- Reynolds, S. P. 1998, *ApJ*, 493, 375
- Reynolds, S. P., Borkowski, K. J., Hwang, U., Hughes, J. P., Badenes, C., Laming, J. M., & Blondin, J. M. 2007, *ApJ*, 668, L135
- Slane, P., Gaensler, B. M., Dame, T. M., Hughes, J. P., Plucinsky, P. P., & Green, A. 1999, *ApJ*, 525, 357
- Smith, R. K., Brickhouse, N. S., Liedahl, D. A., & Raymond, J. C. 2001, *ApJ*, 556, L91
- Smith, R. K., & Hughes, J. P. 2010, *ApJ*, 718, L583
- Uchiyama, Y., & Aharonian, F. A. 2008, *ApJ*, 677, L105
- Vink, J., Laming, J. M., Gu, M. F., Rasmussen, A., & Kaastra, J. S. 2003, *ApJ*, 587, L31
- Vink, J., Bleeker, J., van der Heyden, K., Bykov, A., Bamba, A., & Yamazaki, R. 2006, *ApJ*, 648, L33
- Weaver, R., McCray, R., Castor, J., Shapiro, P., & Moore, R. 1977, *ApJ*, 218, 377
- Xiao, X., & Chen, Y. 2008, *Advances in Space Research*, 41, 416

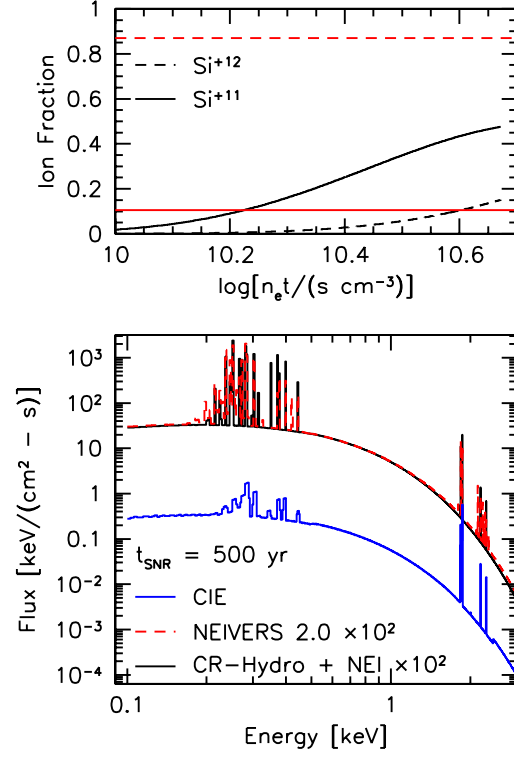


FIG. 1.— *Top Panel:* Evolution of ionization fraction for Si^{+11} and Si^{+12} in a single temperature nonequilibrium ionization calculation up to $t_{\text{SNR}} = 500 \text{ yr}$. The solid and dashed red lines correspond to the collisional ionization equilibrium values for Si^{+11} and Si^{+12} at $T_e = 3 \times 10^6 \text{ K}$. *Bottom Panel:* Thermal X-ray emission line spectrum for a single temperature NEI model at an ionization age of $4.7 \times 10^{10} \text{ s cm}^{-3}$, which corresponds to $t_{\text{SNR}} = 500 \text{ yr}$ and $n_{p,0} = 3.0 \text{ cm}^{-3}$. We only include emission from H, He, and Si. The black curve corresponds to our calculation and is compared directly to an equivalent XSPEC `nei` model at the same ionization age and temperature, which is shown as the red curve. The blue curve corresponds to the emission from a plasma at the same temperature in collisional ionization equilibrium.

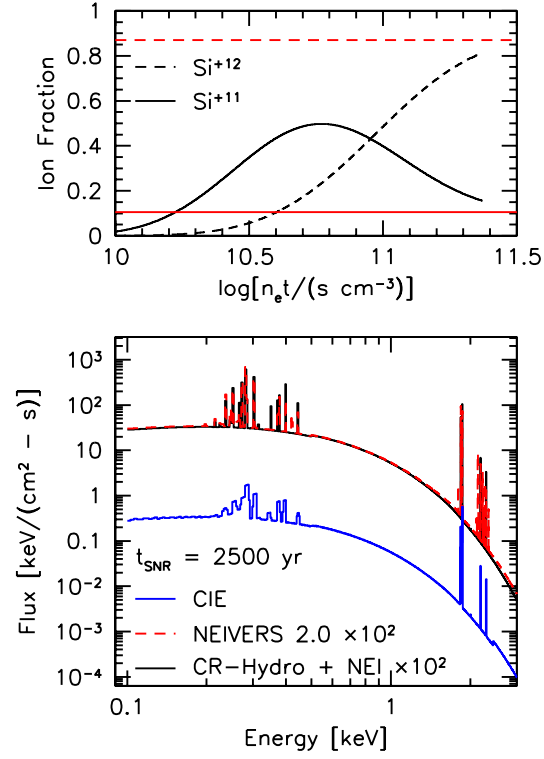


FIG. 2.— *Top Panel:* Evolution of ionization fraction for Si^{+11} and Si^{+12} in a single temperature nonequilibrium ionization calculation up to $t_{\text{SNR}} = 2500$ yr. The solid and dashed red lines correspond to the collisional ionization equilibrium values for Si^{+11} and Si^{+12} at $T_e = 3 \times 10^6$ K. *Bottom Panel:* Thermal X-ray emission line spectrum for a single temperature NEI model at an ionization age of 2.4×10^{11} s cm^{-3} , which corresponds to $t_{\text{SNR}} = 2500$ yr and $n_{p,0} = 3.0 \text{ cm}^{-3}$. We only include emission from H, He, and Si. The black curve corresponds to our calculation and is compared directly to an equivalent XSPEC `nei` model at the same ionization age and temperature, shown here as a red curve. The blue, curve corresponds to the emission from a plasma at the same temperature in collisional ionization equilibrium.

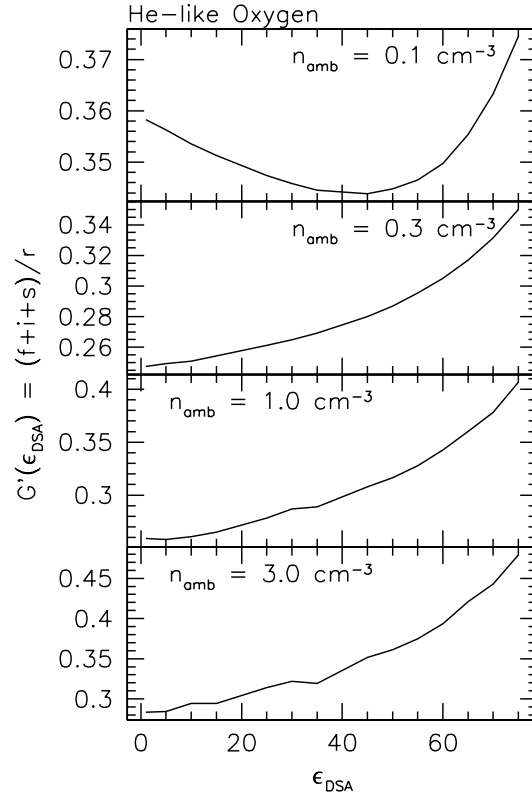


FIG. 3.— G' -ratio for He-like Oxygen in models with $n_{p,0} = 0.1, 0.3, 1.0,$ and 3.0 cm^{-3} versus acceleration efficiency. The G' -ratio is integrated over the entire region between the forward shock and contact discontinuity.

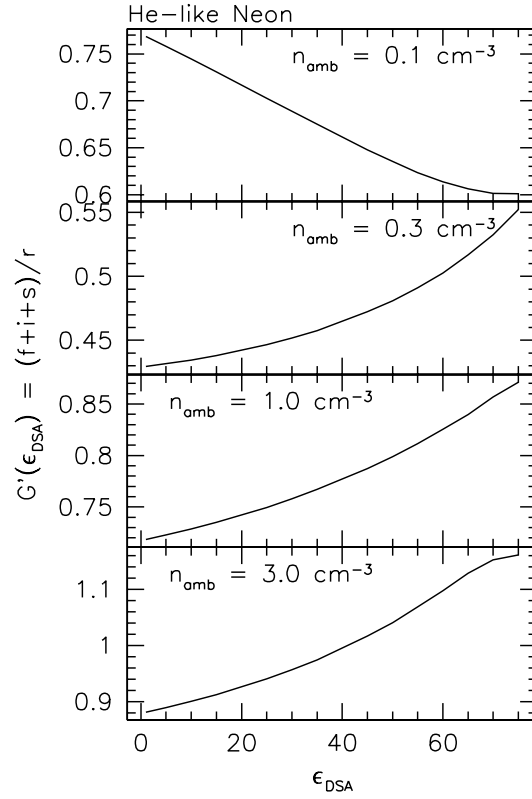


FIG. 4.— G' -ratio for He-like Neon in models with $n_{p,0} = 0.1, 0.3, 1.0,$ and 3.0 cm^{-3} versus acceleration efficiency. The G' -ratio is integrated over the entire region between the forward shock and contact discontinuity.

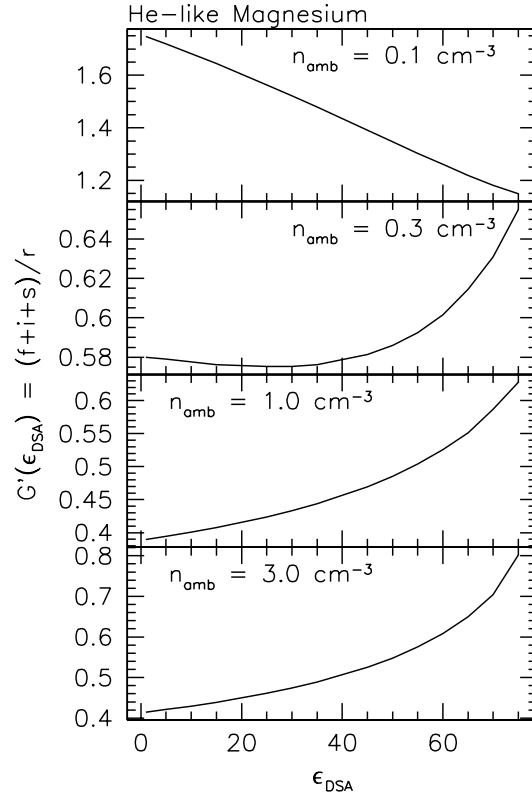


FIG. 5.— G' -ratio for He-like Magnesium in models with $n_{p,0} = 0.1, 0.3, 1.0,$ and 3.0 cm^{-3} versus acceleration efficiency. The G' -ratio is integrated over the entire region between the forward shock and contact discontinuity.

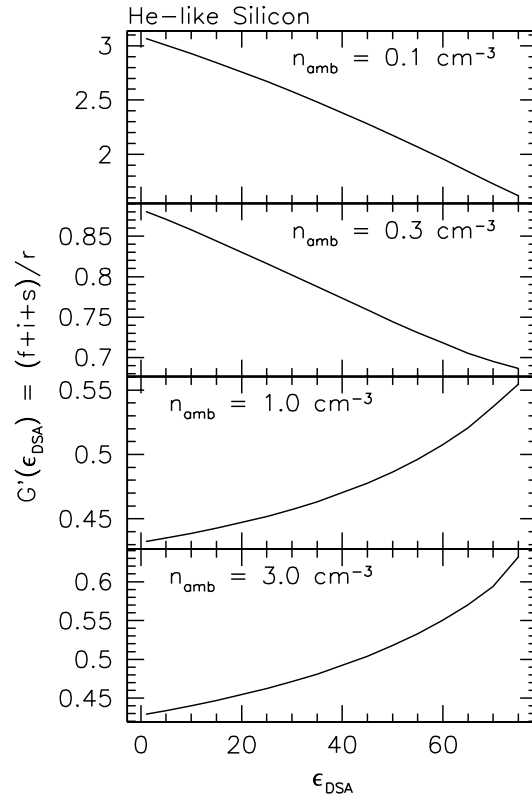


FIG. 6.— G' -ratio for He-like Silicon in models with $n_{p,0} = 0.1, 0.3, 1.0,$ and 3.0 cm^{-3} versus acceleration efficiency. The G' -ratio is integrated over the entire region between the forward shock and contact discontinuity.

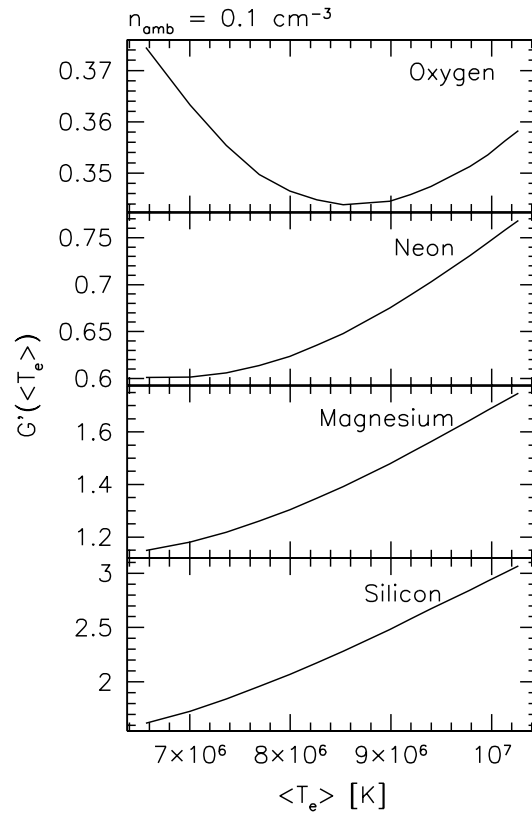


FIG. 7.— G' -ratio as a function of emission measure weighted electron temperature for oxygen, neon, magnesium, and silicon, for an ambient medium density of 0.1 cm^{-3} .

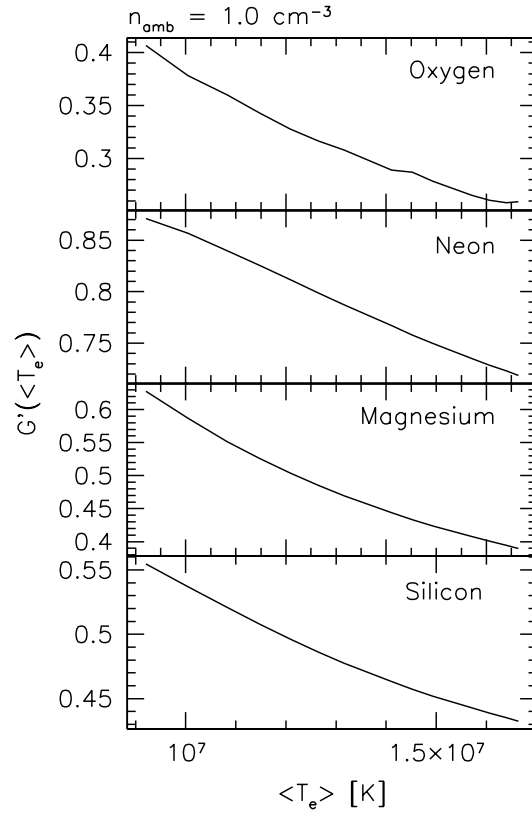


FIG. 8.— G' -ratio as a function of emission measure weighted electron temperature for oxygen, neon, magnesium, and silicon, for an ambient medium density of 1.0 cm^{-3} .

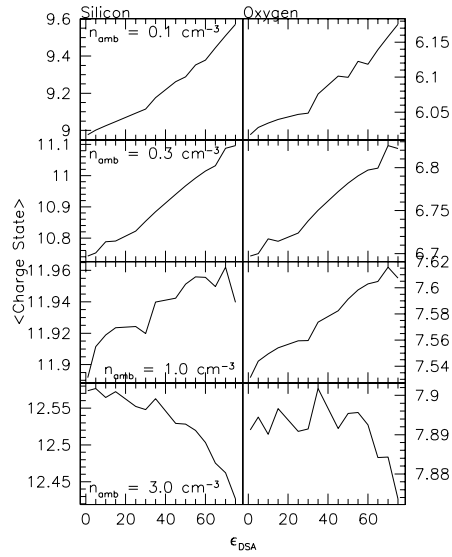


FIG. 9.— Average integrated charge states for silicon (left hand panels) and oxygen (right hand panels) as a function of density and acceleration efficiency. The higher density models show some scatter but, like the lower density models, there appears to be a clear trend with acceleration efficiency.

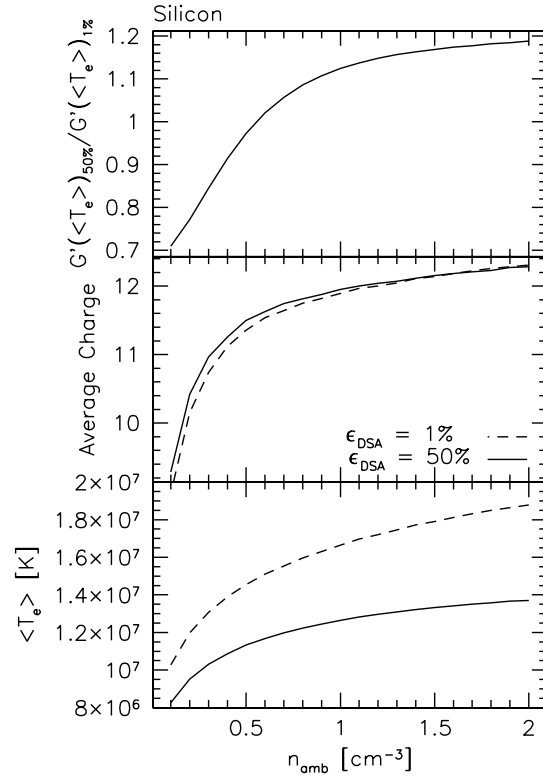


FIG. 10.— *Top*: The ratio of G' for He-like silicon in a 50% efficient model versus a test-particle model for a range of densities between $0.1 - 2.0 \text{ cm}^{-3}$. *Middle*: The average charge state behind the shock for the test-particle and efficient model. *Bottom*: The emission measure weighted electron temperature.

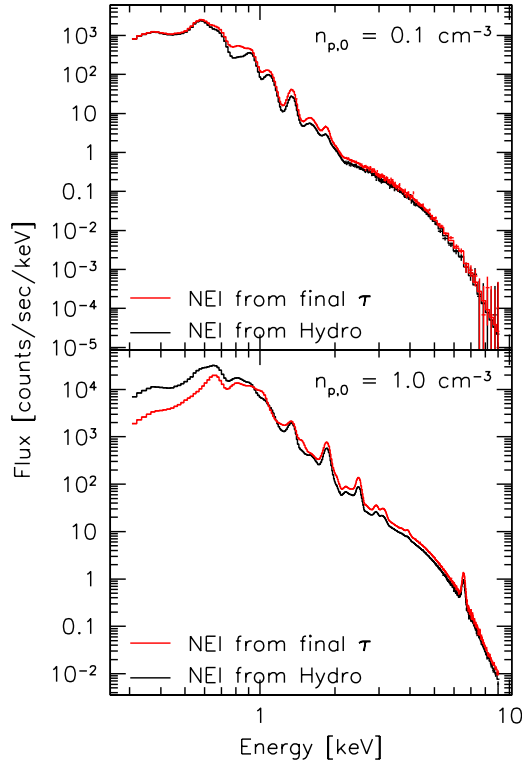


FIG. 11.— *Top*: Simulated *Chandra* ACIS-S X-ray spectrum from a model with $n_{p,0} = 0.1 \text{ cm}^{-3}$ where the ionization is calculated self-consistently with the hydrodynamics (black curve) versus the ionization being calculated after the simulation, based on the final ionization age and temperature (red curve). *Bottom*: Same as in the top panel, but for an ambient medium density of $n_{p,0} = 1.0 \text{ cm}^{-3}$. In both cases, we assume $\epsilon_{\text{DSA}} = 1.0\%$.

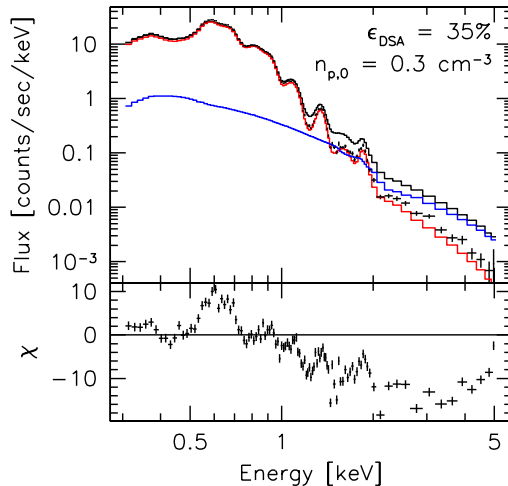


FIG. 12.— Comparison between the emitted thermal X-ray spectrum from a test-particle model versus the combined thermal and nonthermal spectrum from a 35% efficient model, with $n_{p,0} = 0.3 \text{ cm}^{-3}$. The data correspond to the simulated test-particle spectrum, the black curve corresponds to the combined thermal and nonthermal spectrum from the efficient model, the blue curve corresponds to the synchrotron component contribution to the model, and the red curve corresponds to the thermal contribution. The bottom panel shows the difference between the thermal emission from the test particle model (the data) and the model (here, the thermal emission from the efficient model as well as the contribution from the continuum.)